Communications of BAO, Vol. 73, Issue 2, 2026, pp. 394–406

Solar Wind–Magnetosphere MHD Modelling for Geomagnetic Disturbance Studies: An Exposure-Metric Pipeline for Three Historical Solar-Wind Regimes

S. Shamyar *[1], M. Rah[1,2], and A. G. Yeghikyan[1]

[1]MESCS RA V. Ambartsumian Byurakan Astrophysical Observatory (BAO), Armenia
[2]The Silk Road Project at the National Astronomical Observatories, Chinese Academy of Sciences, Beijing, China

Abstract

Whether geomagnetic disturbances (GMDs) influence cardiac arrhythmia is still disputed, and most studies on the question measure exposure with daily planetary indices alone. In this paper, we derive physically based exposure metrics for such studies from magnetohydrodynamic (MHD) simulations; the cardiac hypothesis itself is not tested. We present two-dimensional simulations of three historical solar-wind regimes: a high-speed stream (26 August 1992), a corotating interaction region (November 1993) and a coronal mass ejection (8–9 November 1991). We drive the ideal-MHD code PLUTO 4.4 in the X–Z GSM plane with steady conditions representing each event and sample the field every 14 s at a fixed station on the dipole axis, 4 $R_{\rm E}$ north of the planet. Empirical Dst and Kp proxies computed from the inputs alone place the three drivers in the observed storm classes, within about 12% in Dst for the weakest and strongest events. A scan along the dipole axis shows that the enhancement of the rate of change of the field next to the inner boundary does not extend to the station on the snapshot cadence. The field variability, σ_B = 19.8, 37.1 and 53.2 nT, and the Pc4+Pc5 band power, 4.0, 7.3 and 141 nT^2, increase in the order HSS, CIR, CME, the order of the driving dynamic pressure. The peak dB/dt of 1.9–2.2 nT s^{-1} in the first minute does not follow that order, and we attribute it to the start-up of the run. We discuss the limitations of the two-dimensional model.

Keywords: *solar wind, magnetosphere, geomagnetic disturbances, magnetohydrodynamics, space weather, ULF waves, heliobiology*

1. Introduction

1.1. Space weather and the heart: a disputed literature

Geomagnetic disturbances (GMDs) are variations of the near-Earth magnetic field driven by structures in the solar wind. Their technological consequences are well established: a time-varying field induces a geoelectric field in the conducting ground, which drives geomagnetically induced currents (GICs) through power grids, pipelines and other long conductors (Boteler et al., 1998, Pulkkinen et al., 2017). Whether GMDs also affect human health is a far less settled question.

The epidemiological evidence does not point in one direction. A time-series analysis of daily deaths in 263 cities in the United States found that higher Kp was associated with higher total, cardiovascular, and myocardial-infarction mortality (Zilli Vieira et al., 2019). Small monitoring studies report that heart-rate variability, a marker of autonomic nervous system activity, responds to changes in solar and geomagnetic activity (Alabdulgader et al., 2018, McCraty et al., 2017). For life-threatening arrhythmia, however, the published association has the opposite sign. Reviewing his own and earlier studies, Stoupel (2006) concluded that geomagnetic activity appears to have some protective effect against cardiac arrhythmia and sudden cardiac death. The largest study to date reached the same conclusion from device data: in the ALTITUDE database, with a daily mean of about 59 500 remotely monitored patients between January 2009 and May 2012, the daily rate of implantable cardioverter-defibrillator (ICD) shocks fell from 1.29 per 1000 patients on

*sam.shamyar@gmail.com, Corresponding author

quiet days to 0.94 on storm days (Ebrille et al., 2015). Positive associations for mortality and inverse associations for device-treated arrhythmia are not necessarily in conflict, since they concern different endpoints, but together they show that the sign of any effect on arrhythmia cannot be assumed in advance.

These studies share one limitation. Exposure is measured with planetary indices such as Kp and Ap, which summarise global activity over three hours or a day (Matzka et al., 2021). They do not record the rate of change of the field or its ultra-low-frequency (ULF) content, the two quantities through which a physical coupling to biological tissue would most plausibly act. A test of the arrhythmia hypothesis, therefore, needs exposure metrics that are tied to the physics of the solar wind–magnetosphere interaction and that can be computed for specific events.

1.2. Previous work and aim of this paper

A pilot MHD simulation of a single regime, a high-speed stream, was presented at the 17th International Solar Wind Conference (Bath, United Kingdom, 14–19 June 2026; poster 2-087) (Shamyar et al., 2026). That simulation used a coarse grid and sampled its diagnostics only at the cadence of the output snapshots, which is too coarse to resolve the rate of change of the field. It showed that the pipeline runs from the solar-wind input to synthetic field, dB/dt and ULF diagnostics at virtual stations, and that the simulated flow has the expected qualitative structure, but it made no claim about calibrated physical magnitudes.

In this paper, we extend the simulations to three historical events that span weak to extreme driving, and we sample the station diagnostics at high cadence. We also add two checks: a comparison of the adopted drivers with the observed Dst and Kp indices and a check of the influence of the inner boundary at the location of the diagnostic station. The paper deals only with the physics, namely the construction and checking of the pipeline that turns solar-wind conditions into exposure metrics; it does not analyse clinical data.

2. Background

2.1. Three solar-wind drivers of geomagnetic disturbance

Geomagnetic storms develop when the interplanetary magnetic field (IMF) stays southward for long enough to drive a sustained dawn–dusk electric field across the magnetosphere (Gonzalez et al., 1994). Two kinds of solar-wind structures supply such conditions. Coronal mass ejections (CMEs) are transient eruptions whose shocks, sheaths, and ejecta can carry strong, long-lasting southward IMF; they produce the most intense storms. High-speed streams (HSSs) from coronal holes, and the corotating interaction regions (CIRs) that form where a fast stream overtakes slower wind, recur with the solar rotation and produce weak to moderate but long-lived activity (Tsurutani et al., 2006). The two classes differ systematically in almost every aspect of the magnetospheric response (Borovsky & Denton, 2006). We therefore treat an HSS, a CIR and a CME as three regimes that an exposure model must cover.

2.2. Arrhythmia burden and the ICD as a sensor

Arrhythmia burden denotes how often and how severely a patient experiences abnormal heart rhythms. An ICD monitors the cardiac rhythm continuously and treats ventricular tachyarrhythmia with antitachycardia pacing or a shock. Each therapy is stored with its time, and remote-monitoring networks collect these records from very large patient populations (Saxon et al., 2010). Device records therefore provide objective, time-stamped arrhythmic events against which an environmental exposure can be tested. They have been used in this way for air pollution, with a case-crossover design (Maclure, 1991) in which each patient serves as their own control (Rich et al., 2005). The same design can be applied to geomagnetic exposure (Section 5.2).

2.3. A proposed physical pathway

The hypothesis that motivates this work is a chain of four links: (i) a solar-wind structure perturbs the magnetosphere; (ii) the perturbation appears as a rate of change of the field, dB/dt, and as ULF power in the Pc3–Pc5 bands (Jacobs et al., 1964); (iii) these variations modulate autonomic regulation of the heart; (iv) in patients with a vulnerable substrate, that modulation alters the probability of arrhythmia. Links (i) and (ii) are standard magnetospheric physics. Link (iii) rests at present on small studies. McCraty

doi: https://doi.org/10.52526/25792776-26.73.2-394

et al. (2017) monitored ten participants for 31 days and reported that their heart-rate-variability rhythms synchronised with one another and correlated with solar and geomagnetic variables, and Alabdulgader et al. (2018) reported related correlations for 16 participants followed over five months. We regard link (iii) as a hypothesis that motivates the choice of metrics, not as an established mechanism. Nothing in this paper tests links (iii) or (iv).

3. Methods

3.1. Event selection and driving parameters

The three events were chosen from the OMNI near-Earth solar-wind record (King & Papitashvili, 2005): an HSS on 26 August 1992, a CIR in November 1993 during the early-November 1993 storm interval, in which a corotating interaction region together with solar-wind transients started the storm, and a high-speed stream prolonged it (Knipp et al., 1998); and the CME-driven great storm of 8–9 November 1991. Each is represented by a single set of steady upstream values of proton number density n, speed V and IMF north–south component B_z (Table 1). These are representative values for each interval, chosen with reference to the OMNI record; they are not averages over a formally defined time window, and we treat them as idealised drivers of each class. From these, we derive the dynamic pressure and the dawn–dusk electric field,

$$P_{\mathrm{dyn}} = m_{\mathrm{p}}\, n V^2, \qquad E_y = V B_{\mathrm{s}}, \qquad B_{\mathrm{s}} = \max(-B_z,\, 0), \tag{1}$$

where m_{p} is the proton mass. With n in cm^{-3}, V in km s^{-1} and B_{s} in nT, these give P_{dyn} in nPa as $1.6726 \times 10^{-6}\, nV^2$ and E_y in mV m^{-1} as $10^{-3}\, V B_{\mathrm{s}}$. The observed indices used for comparison are the final Dst index of the World Data Center for Geomagnetism, Kyoto (Nose et al., 2015), and the Kp index of GFZ Potsdam (Matzka et al., 2021).

Table 1. Steady upstream conditions adopted for the three regimes, the derived driving quantities of Eq. (1), and the observed minimum hourly Dst (WDC Kyoto) and approximate Kp (GFZ Potsdam) for the event days. For the CIR event the listed Dst is not the minimum of the storm interval, which reached −119 nT on 4 November 1993 (Nose et al., 2015).

	HSS	CIR	CME
Event date	26 Aug 1992	Nov 1993	8–9 Nov 1991
n [cm^{-3}]	9.90	14.99	12.00
V [km s^{-1}]	405	500	750
B_z [nT]	−4.01	−6.00	−20.02
P_{dyn} [nPa]	2.72	6.27	11.29
E_y [mV m^{-1}]	1.62	3.00	15.02
Observed Dst [nT]	−40	−50	−354
Observed Kp	4− (3.67)	≈4–5	9− (8.67)

3.2. MHD model

We solve the equations of ideal MHD with the PLUTO code, version 4.4 (Mignone et al., 2007, 2012), which has previously been applied to the response of the terrestrial magnetosphere to extreme solar wind (Varela et al., 2022). The computation is two-dimensional and Cartesian, in the X–Z plane of the geocentric solar magnetospheric (GSM) system, with x_1 pointing sunward and x_2 northward. Lengths are normalised to the Earth radius, $R_{\mathrm{E}} = 6371$ km, velocities to $v_0 = 450$ km s^{-1} and number densities to $n_0 = 5$ cm^{-3}. The units of magnetic field, pressure and time that follow are $B_0 = v_0(\mu_0 m_{\mathrm{p}} n_0)^{1/2} = 46.12$ nT, $p_0 = m_{\mathrm{p}} n_0 v_0^2 = 1.69$ nPa and $t_0 = R_{\mathrm{E}}/v_0 = 14.16$ s.

The planetary field is a dipole centred on the origin. The domain is filled at $t = 0$ with the uniform solar wind of Table 1, flowing in the $-x_1$ direction and carrying the IMF B_z. The driving is steady: the upstream conditions do not change during a run. The planet is represented by an internal boundary: inside $r \le 1\ R_{\mathrm{E}}$ the density and pressure are reset at every time step to 100 and 10 code units (about 500 cm^{-3} and

17 nPa) and the velocity to zero. The domain covers $-40 \le x_1, x_2 \le 40\ R_E$ on a uniform grid of 128×128 cells (cell size 0.625 R_E). The equations are solved with the HLL Riemann solver (Harten et al., 1983), piecewise-linear reconstruction and second-order Runge–Kutta time stepping, with a Courant number of 0.25, and the divergence of the magnetic field is controlled with the eight-wave formulation (Powell et al., 1999). The solar-wind values of Table 1 are held fixed in the ghost cells at $x_1 = -40\ R_E$, and zero-gradient conditions are applied at the other three outer boundaries. Since the flow is directed towards $-x_1$, the solar wind enters through the boundary at $x_1 = +40\ R_E$, where the zero-gradient condition preserves the undisturbed upstream state of the initial condition. The dipole moment is directed along $+x_2$, and the dipole strength is $B_d = 8$ code units, i.e. 369 nT on the equator at 1 R_E. The thermal pressure of the solar wind is 0.012 code units for the HSS and CIR runs and 0.005 for the CME run. Each run lasts 200 time units, or 47.2 min. The full two-dimensional state is written every 20 time units (283 s), giving 11 snapshots per run.

Two properties of this set-up govern how the results should be read, and we state them here once. First, each run is an initial-value problem that starts impulsively: at $t = 0$ the solar wind already fills the domain and meets the dipole and the over-pressured core, so the first minutes contain the adjustment to that initial state. Secondly, the inner boundary is an idealised obstacle that is re-imposed continuously and does not respond to the flow. The time series at the station therefore describe the response of this model at this point. They are not a reconstruction of the field that was observed during the historical events. Section 5.1 returns to both points.

3.3. Station diagnostics and exposure metrics

A virtual station is placed on the dipole axis at $(x_1, x_2) = (0, +4)\ R_E$, 4 R_E north of the planet. The field components B_x and B_z in the cell nearest to this point are recorded once per time unit, so that each run yields about 200 samples at a median spacing Δt of 14.16–14.25 s. No smoothing or interpolation is applied. Four quantities are derived from this series. The field magnitude is

$$|B|(t) = \left(B_x^2 + B_z^2\right)^{1/2}, \tag{2}$$

and its rate of change is taken as the magnitude of the vector time derivative, estimated by first-order differences between consecutive samples,

$$\frac{dB}{dt} = \left[\left(\frac{\Delta B_x}{\Delta t}\right)^2 + \left(\frac{\Delta B_z}{\Delta t}\right)^2\right]^{1/2}. \tag{3}$$

This has the same form as the time derivative of the horizontal ground field used as an indicator of GIC activity (Pulkkinen et al., 2013, Viljanen et al., 2001), applied here to the two field components of the model plane; it retains changes in direction that the derivative of $|B|$ would miss. The overall variability of a run is summarised by the standard deviation of the N samples,

$$\sigma_B = \left[\frac{1}{N}\sum_{i=1}^{N}\left(|B|_i - \langle|B|\rangle\right)^2\right]^{1/2}. \tag{4}$$

Finally, the power spectral density $S(f)$ of the mean-subtracted $|B|$ series is estimated by Welch's method (Welch, 1967) with a Hann window and segments of 64 samples, and is integrated over a frequency band to give the band power,

$$P_{\mathrm{band}} = \int_{f_1}^{f_2} S(f)\, df. \tag{5}$$

The sampling interval sets the Nyquist frequency at about 35 mHz and the segment length sets the frequency resolution at 1.1 mHz. In the classification of Jacobs et al. (1964), Pc5 covers periods of 150–600 s (1.7–6.7 mHz), Pc4 45–150 s (6.7–22 mHz) and Pc3 10–45 s (22–100 mHz). We quote the combined Pc4+Pc5 power with $f_1 = 2$ mHz and $f_2 = 22$ mHz. This band covers Pc4 completely and Pc5 down to 2 mHz; the part of Pc5 below 2 mHz is narrower than one frequency bin (1.1 mHz). Only the lowest part of Pc3 is reached, and we make no statement about Pc3.

The plasma density, the flow speed and the signed B_z at the station, and the field at other radial distances, are not part of the high-cadence station output. They are taken from the 11 snapshots and so have a cadence of 283 s.

3.4. Index proxies for the drivers

Before any simulation output is used, we ask whether the adopted inputs are consistent with the observed severity of each event. Two kinds of empirical model, which need only the quantities of Eq. (1), provide the check.

For Dst we use the model of O'Brien & McPherron (2000), in which the pressure-corrected index Dst* obeys

$$\frac{d\,\mathrm{Dst}^*}{dt} = Q - \frac{\mathrm{Dst}^*}{\tau}, \qquad Q = -a\,(E_y - E_\mathrm{c}), \qquad \tau = \tau_0 \exp\!\left(\frac{E_1}{E_2 + E_y}\right), \tag{6}$$

where the coefficients carry the units that make each term dimensionally consistent: $a = 4.4$ nT h^{-1} (mV m^{-1})$^{-1}$, $E_\mathrm{c} = 0.5$ mV m^{-1}, $\tau_0 = 2.40$ h, $E_1 = 9.74$ mV m^{-1} and $E_2 = 4.69$ mV m^{-1}. With E_y in mV m^{-1}, Q is thus in nT h^{-1} and τ in hours, and $Q = 0$ for $E_y \le E_\mathrm{c}$. The index itself is recovered from $\mathrm{Dst} = \mathrm{Dst}^* + b\,P_\mathrm{dyn}^{1/2} - c$, with $b = 7.26$ nT nPa$^{-1/2}$ and $c = 11$ nT. O'Brien & McPherron (2000) give $E_\mathrm{c} = 0.49$ mV m^{-1}; the difference changes none of the values quoted below by more than 0.5 nT. For steady driving that starts from $\mathrm{Dst}^* = 0$, Eq. (6) integrates to $\mathrm{Dst}^*(T) = Q\tau\,(1 - e^{-T/\tau})$ after a time T.

O'Brien & McPherron (2000) restricted their analysis to Dst > -150 nT, so its use for the CME event is an extrapolation. For that event we also evaluate the modified form of the formula of Burton et al. (1975) given by Fenrich & Luhmann (1998), with a pressure-dependent injection term and a faster decay under strong driving:

$$Q = -a'\,(E_y - E_\mathrm{c})\,P_\mathrm{dyn}^{1/3}, \qquad \tau = \begin{cases} 7.7\ \mathrm{h}, & E_y \le 4\ \mathrm{mV\ m^{-1}} \\ 3\ \mathrm{h}, & E_y > 4\ \mathrm{mV\ m^{-1}} \end{cases}, \qquad \mathrm{Dst} = \mathrm{Dst}^* + b'\,P_\mathrm{dyn}^{1/2} - c', \tag{7}$$

with $a' = 4.32$ nT h^{-1} (mV m^{-1})$^{-1}$ nPa$^{-1/3}$, $E_\mathrm{c} = 0.5$ mV m^{-1}, $b' = 15.8$ nT nPa$^{-1/2}$ and $c' = 20$ nT, so that Q is again in nT h^{-1} for E_y in mV m^{-1} and P_dyn in nPa. For the May 2024 superstorm, Liu et al. (2024) noted that the Burton formulation tends to overestimate and the O'Brien–McPherron formulation to underestimate the depth of the storm, and they averaged the two. We follow that practice for the CME event and quote both members of the pair.

For Kp we use the coupling-function fit of Newell et al. (2008),

$$\mathrm{Kp} = 0.05 + 2.244 \times 10^{-4}\,\frac{d\Phi_\mathrm{MP}}{dt} + 2.844 \times 10^{-6}\,n^{1/2}V^2, \qquad \frac{d\Phi_\mathrm{MP}}{dt} = V^{4/3}B_\mathrm{T}^{2/3}\sin^{8/3}\!\left(\frac{\theta_\mathrm{c}}{2}\right), \tag{8}$$

where B_T is the transverse IMF magnitude and θ_c the IMF clock angle (Newell et al., 2007). Here V is in km s^{-1}, B_T in nT and n in cm^{-3}, the units for which the coefficients were fitted, and Kp is dimensionless. Since only B_z is specified, we take the IMF to be purely southward, $B_\mathrm{T} = |B_z|$ and $\theta_\mathrm{c} = 180°$. The result is limited to the range 0–9 of the index.

4. Results

4.1. Consistency of the drivers with observed Dst and Kp

Fig. 1 and Table 2 compare the proxies of Section 3.4 with the observed indices. This comparison uses the three input values of each event and nothing else. It is independent of the MHD computation and of every limitation of that computation.

For the CME event the two Dst formulations give -237 and -389 nT after 24 h, by which time both are within 1 nT of their asymptotes. They bracket the observed minimum of -354 nT, and their mean, -313 nT, is 12% smaller in magnitude. For the HSS event, 12 h of steady driving gives -35 nT against an observed -40 nT, a difference of 11%. For these two events the proxy reproduces the observed depth of the storm to within about 12%.

The CIR event shows the weakness of a steady-state check. Because the decay time τ is 8.5 h, the proxy has not saturated on the time scale over which a CIR keeps the IMF southward, and the result depends on the assumed duration T. Franco et al. (2026) found that more than 80% of the most energetic periods of IMF B_z fluctuation in CIR-driven storms are shorter than 4 h. With $T = 4$ h the proxy is -28 nT; with $T = 8$ and 12 h it is -50 and -64 nT. The observed -50 nT lies inside this range, but our scalar inputs do not fix T, so for this event the comparison shows consistency and no more. The same reservation applies, more weakly, to the HSS event, for which the asymptotic value is -55 nT.

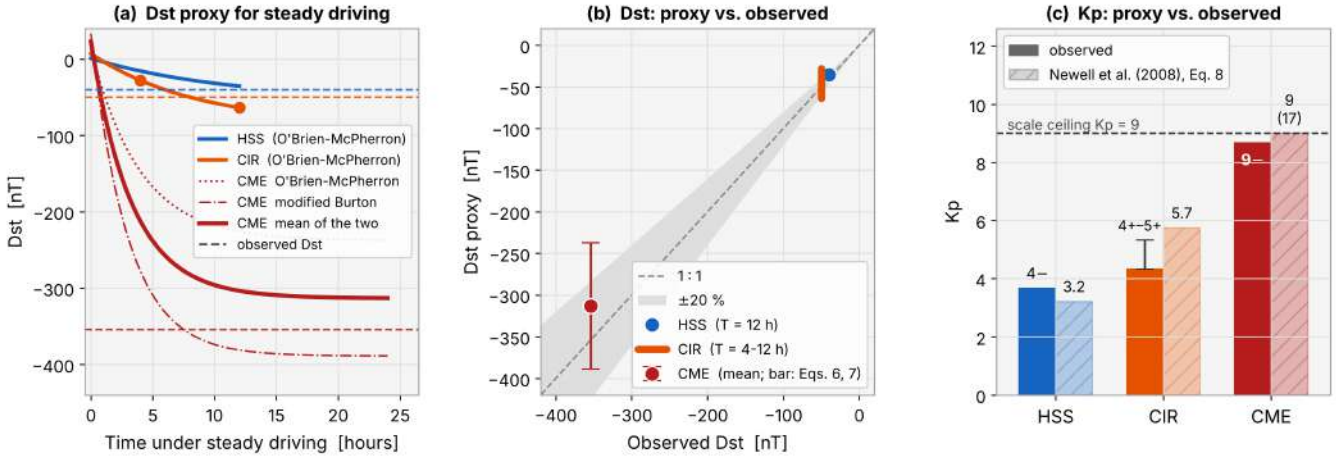

Figure 1. Index proxies computed from the driving parameters of Table 1. (a) Dst proxy as a function of the duration of steady driving. Solid blue and orange curves: Eq. (6) for the HSS and CIR events; the orange circles mark $T = 4$ and 12 h. Red curves: Eq. (6) (dotted), Eq. (7) (dash-dotted) and their mean (solid) for the CME event. Dashed horizontal lines: observed Dst of each event (Table 1). (b) Dst proxy against observed Dst. The orange bar spans $T = 4$–12 h for the CIR event and the red bar spans the two formulations for the CME event. (c) Observed Kp and the proxy of Eq. (8); the whisker on the CIR bar spans the observed range 4+ to 5+. For the CME event the proxy exceeds the ceiling of the index; the unlimited value is given in parentheses.

Table 2. Index proxies and observed values. T is the assumed duration of steady driving. For the CME event the two Dst formulations are listed with their mean. The Kp value in parentheses is the proxy value before limitation to the range of the index.

Quantity	Model	HSS	CIR	CME
τ [h]	Eq. (6)	11.2	8.5	3.9
Dst proxy [nT]	Eq. (6)	-35 ($T = 12$ h)	-28, -50, -64 ($T = 4$, 8, 12 h)	-237 ($T = 24$ h)
	Eq. (7)	–	–	-389 ($T = 24$ h)
	mean	–	–	-313
Dst observed [nT]		-40	-50	-354
Kp proxy	Eq. (8)	3.2	5.7	9 (16.9)
Kp observed		4− (3.67)	≈4–5	9− (8.67)

The Kp proxy of Eq. (8) gives 3.2 for the HSS event, against an observed 4− (3.67), and 5.7 for the CIR event, against approximately 4–5 (4+ to 5+). It thus reproduces the HSS value to within half a Kp unit and lies 0.4–1.4 units above the CIR values. For the CME event it gives 16.9, far above the top of the scale, so the limited value of 9 matches the observed 9− (8.67) only in the sense that the event lies at the ceiling of the index. That agreement carries no quantitative information.

We conclude that the adopted drivers are representative of a weak, a moderate and an extreme event, in that order. We do not claim more for this step. It checks the inputs to the simulation; it says nothing about the realism of the simulated magnetosphere.

4.2. Verification of the station location

The inner boundary resets the plasma state at every step, and a diagnostic placed too close to it would record that forcing instead of the response to the solar wind. To see how far its influence reaches we computed, from the 11 snapshots, the peak rate of change of $|B|$ in six grid cells along the dipole axis, centred at $x_1 = -0.31\ R_E$ and $x_2 = 0.94$, 2.19, 2.81, 4.06, 4.69 and 5.94 R_E (Fig. 2). The innermost cell lies at $r = 0.99\ R_E$, at the edge of the inner boundary, and the fourth is the cell of the station.

In the innermost cell, at the edge of the boundary, the peak is 2.3 nT s^{-1} in all three runs. At 2.2 R_E it

doi: https://doi.org/10.52526/25792776-26.73.2-394

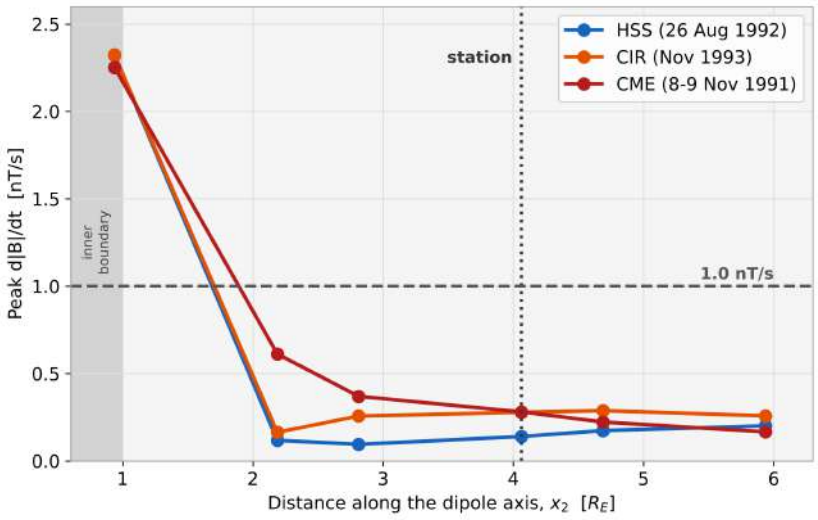

Figure 2. Peak rate of change of $|B|$ between consecutive snapshots (cadence 283 s) in six grid cells along the dipole axis, for the three regimes. The grey band marks the inner boundary ($r \leq 1\ R_{\mathrm{E}}$), the dotted vertical line the cell of the diagnostic station and the dashed horizontal line the 1 nT s^{-1} reference level of Fig. 4.

has fallen to 0.12, 0.16 and 0.61 nT s^{-1} for the HSS, CIR and CME runs, lower by factors of about 20, 14 and 4. From 2.2 to 5.9 R_{E} the values stay between 0.09 and 0.61 nT s^{-1}, with no systematic trend and no consistent ordering of the regimes. At the station they are 0.14, 0.28 and 0.28 nT s^{-1}, at least eight times smaller than at the edge of the boundary in every run.

The enhancement produced by the boundary is thus confined to its immediate neighbourhood on the snapshot cadence, and the station lies outside it. Two reservations apply. The snapshot cadence cannot resolve changes faster than a few minutes: at the station the same quantity computed from the 14 s series is about an order of magnitude larger (Section 4.4), so the scan says nothing about short transients. And the profile, taken along the dipole axis only, is a property of this model with its idealised obstacle. It should not be read as the dependence of dB/dt on distance in the real magnetosphere.

4.3. Field evolution at the station

Fig. 3 shows $|B|(t)$ at the station. All three runs begin with a rise from 5–10 nT to 84–92 nT within the first 2–4 min. After that they diverge.

In the HSS run the field peaks at about 84 nT near $t = 2$ min and then decays steadily; it has fallen to about 10 nT by 10 min and is below 1 nT after 20 min. In the CIR run a first maximum of 92 nT at 2 min is followed by a plateau of 80–90 nT that lasts until about 12 min, a decline to nearly zero at 33 min, and a second rise that reaches 103 nT at the end of the run. In the CME run a first maximum of 91 nT at 4 min is followed by a collapse to about 10 nT at 7 min, after which the field grows without interruption to 211 nT. It is still rising when the run stops, so the CME run has not reached a steady state within 47 min. The standard deviations are $\sigma_B = 19.8$, 37.1 and 53.2 nT for the HSS, CIR and CME runs (Table 3).

4.4. Rate of change of the field

The rate of change computed from Eq. (3) is shown in Fig. 4. The dashed lines at 1 and 2 nT s^{-1} are reference levels for the eye. For comparison, the community validation of geospace models for GIC applications used event thresholds of 0.3, 0.7, 1.1 and 1.5 nT s^{-1} for the horizontal field at ground stations (Pulkkinen et al., 2013), while the levels proposed for extreme-GIC alerts are one to two orders of magnitude higher (Kataoka & Ngwira, 2016). Our values refer to a point in the model magnetosphere, not to the ground, so the comparison is one of scale only. We know of no established biological threshold expressed in dB/dt, and the lines should not be read as one.

All three runs exceed 1 nT s^{-1} within the first minute. The maxima are 1.88, 2.21 and 1.97 nT s^{-1} for the HSS, CIR and CME runs, and only the CIR run exceeds 2 nT s^{-1}. At $t = 2$ min every run is below 0.3 nT s^{-1}, and between 2 and 10 min the HSS and CIR runs stay below 0.4 nT s^{-1}. The CME run has a

doi: https://doi.org/10.52526/25792776-26.73.2-394

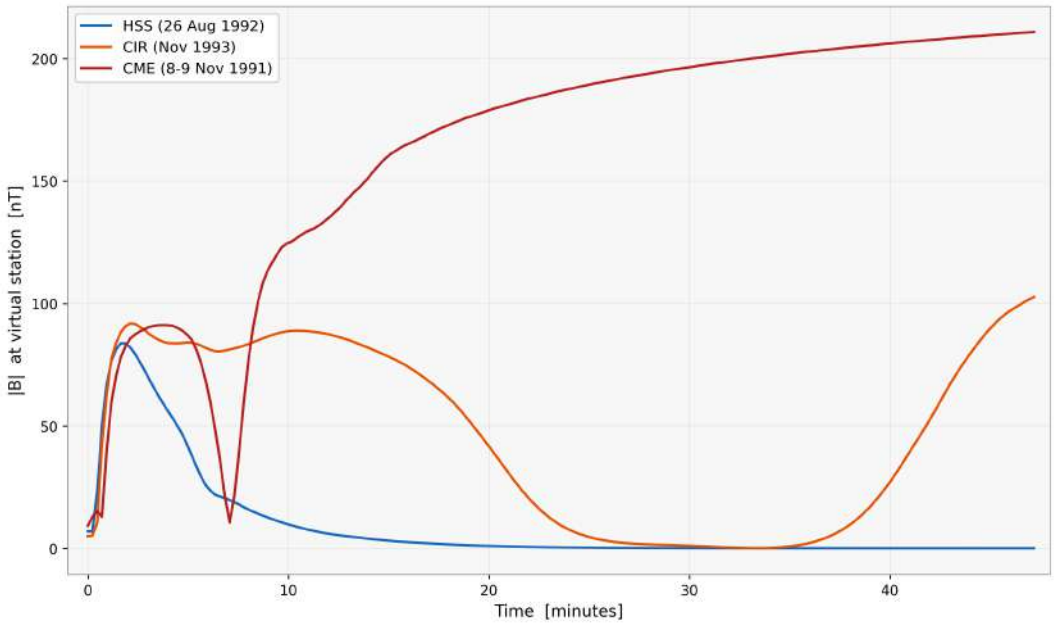

Figure 3. Field magnitude $|B|$ at the diagnostic station, Eq. (2), sampled every 14 s, for the HSS (blue), CIR (orange) and CME (red) runs.

second peak of about 1.4 nT s^{-1} near 7.5 min, during the recovery from the field minimum seen in Fig. 3. After 10 min no run exceeds 0.3 nT s^{-1}.

The three maxima of the first minute differ by less than 20% although the dynamic pressure varies by a factor of 4.2, and their order (CIR, CME, HSS) is not the order of the driving. The CME run, with the fastest wind, also reaches its maximum latest. A response controlled by the solar wind would show neither feature. We therefore attribute this first spike to the impulsive start of the run, that is, to the adjustment between the initial uniform flow, the dipole and the over-pressured core. It should not be used as a measure of event severity, and we draw no physical conclusion from the order of the three peaks.

4.5. Spectral content and integrated metrics

Fig. 5 shows the power spectral density of the three series. Each spectrum falls steeply with frequency, by more than five orders of magnitude between 1 and 35 mHz. The CME spectrum lies above the other two at every resolved frequency, by factors of about 8 and 20 near 2 mHz and, above 5 mHz, by more than an order of magnitude at every frequency and by two orders or more at most frequencies. The HSS and CIR spectra are close to each other and cross several times.

A caution is needed about the meaning of these spectra. The series of Fig. 3 are non-stationary: they consist of a few large, slow excursions, not of sustained oscillations. Their spectra are those of transients and trends, and the band power of Eq. (5) measures how much of the variance of each run falls on time scales of 45 s to 8 min. It is not evidence that the model contains Pc4 or Pc5 pulsations in the sense of magnetospheric wave modes.

With that understanding, Fig. 6 and Table 3 collect the two integrated metrics. The Pc4+Pc5 band power is 4.0, 7.3 and 141 nT^2 for the HSS, CIR and CME runs; the CME value is 19 times the CIR value and 35 times the HSS value. Both σ_B and the band power increase in the order HSS, CIR, CME, which is also the order of P_{dyn} and of E_y (Table 1). The sign of this dependence agrees with observation: Pc5 power in the magnetosphere and on the ground increases with solar-wind speed and with dynamic pressure and its fluctuations (Kepko et al., 2002, Mathie & Mann, 2001, Takahashi & Ukhorskiy, 2007). Three runs cannot establish a scaling law, and we claim only the ordering. The metrics that integrate over the whole run therefore behave as expected, whereas the single largest value of dB/dt does not.

4.6. Density, flow and signed B_z at the station

Fig. 7 adds the plasma density, the flow speed and the signed B_z at the station, taken from the snapshots. Because of the coarser cadence, the $|B|$ panel of this figure does not reproduce the fast features of Fig. 3;

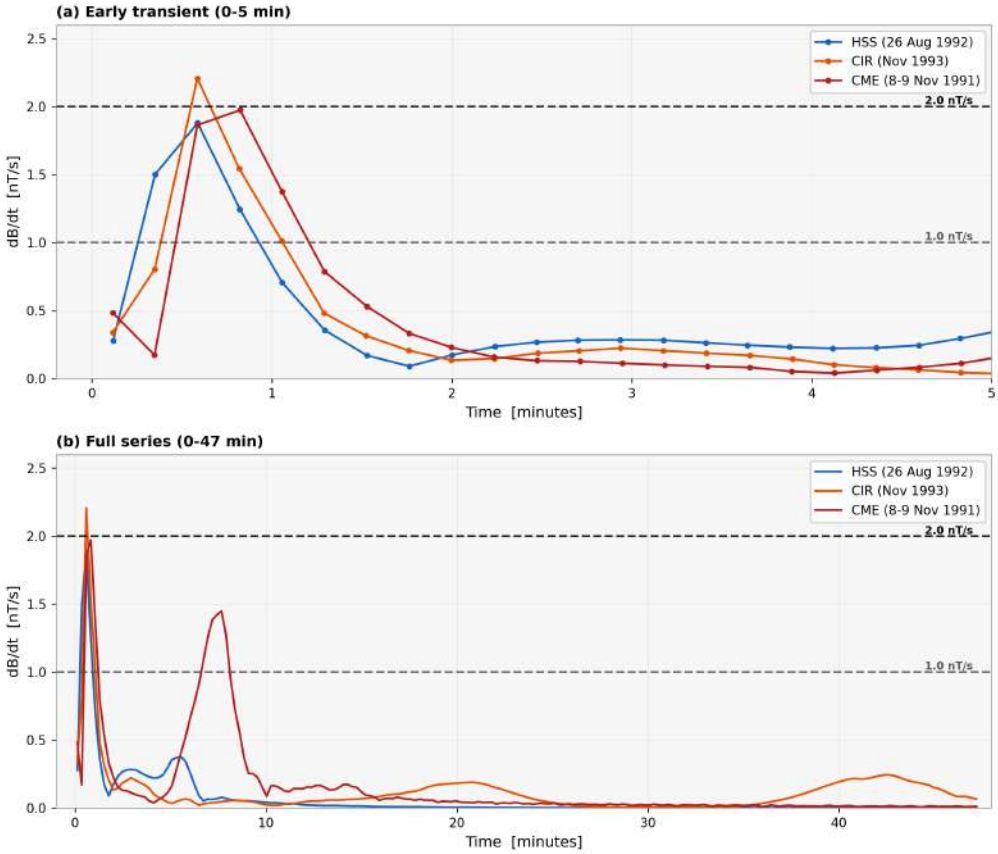

Figure 4. Rate of change of the field at the station, Eq. (3). (a) The first 5 min at full resolution. (b) The whole run. Dashed lines mark the reference levels of 1 and 2 nT s^{-1} discussed in the text.

the latter is the reference for the field. The upstream IMF values are those listed in the key.

The flow at the station slows sharply within the first snapshot interval, from 405, 500 and 750 km s^{-1} to 104, 137 and 157 km s^{-1} in the HSS, CIR and CME runs. This is a local effect. Far from the planet the flow keeps its upstream value throughout, so the driver is unchanged. The density follows three different courses. In the HSS run it rises from 9.9 to about 43 cm^{-3} near 19 min and settles near 33 cm^{-3}. In the CIR run it oscillates strongly, with maxima near 100 cm^{-3} at 9 min and 157 cm^{-3} at 38 min. In the CME run it peaks at 54 cm^{-3} in the first snapshot interval and then falls to 6 cm^{-3} while the field grows.

The most informative panel is that of B_z. In the HSS run B_z rises from +6.8 to +34 nT and decays to zero without changing sign. In the CIR run it rises to +51 nT, decays, and crosses zero between 33 and 38 min, ending at −64 nT. In the CME run it starts at −9 nT, reverses to +57 nT in the first snapshot interval, reverses again to −87 nT in the second, and strengthens to −135 nT at the end. These reversals explain the minima of $|B|$ in Fig. 3: the CME minimum at 7 min and the CIR minimum at 33 min both fall where B_z passes through zero. The field at the station is therefore not simply compressed. It changes polarity, and the late growth in the CIR and CME runs is a build-up of southward field at the station.

Density and flow speed at the station are further candidate exposure variables, subject to the same reservations as the field.

5. Discussion

5.1. Limitations of the present model

The limitations of this work are substantial and bear directly on how the metrics may be used.

Two-dimensional geometry. A model confined to the X–Z plane has no azimuthal direction. It cannot contain the ring current that Dst measures, nor the field-aligned and ionospheric currents that produce most of the ground dB/dt relevant to GICs. Predictions of ground perturbations for operational use are obtained from three-dimensional global MHD models coupled to an ionosphere, or from empirical models (Pulkkinen et al., 2013). The Dst and Kp proxies of this paper characterise the drivers. They are not outputs of the simulation.

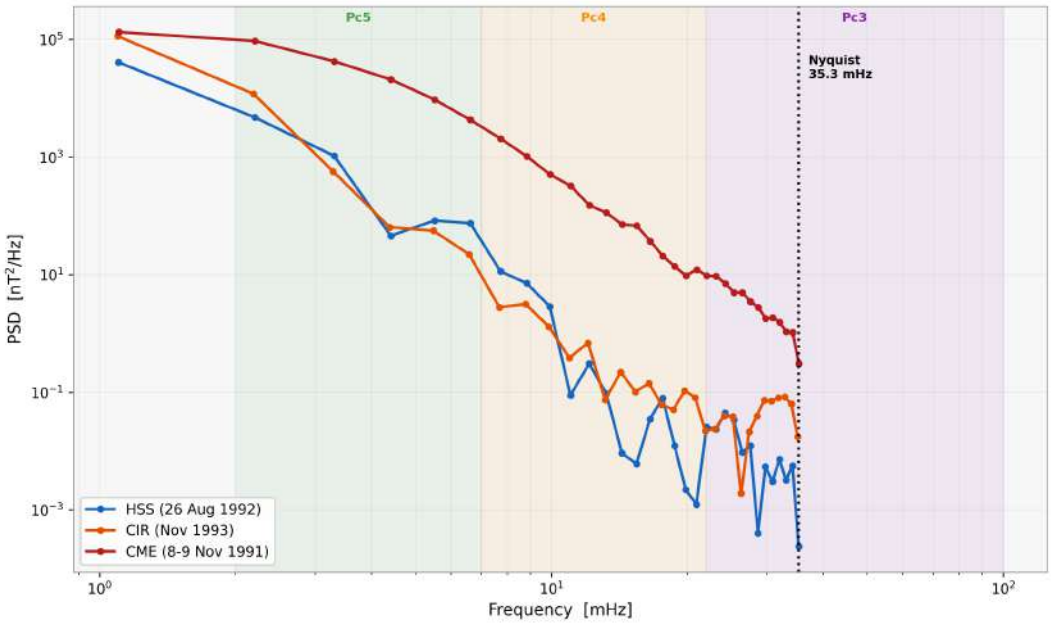

Figure 5. Welch power spectral density of $|B|$ at the station. Shading marks the Pc5, Pc4 and Pc3 bands, with limits rounded to 2, 7, 22 and 100 mHz; the dotted line is the Nyquist frequency of the 14 s sampling, above which nothing is resolved.

Table 3. Exposure metrics at the station for the three regimes. Times of the maxima of dB/dt are those of the plotted samples in Fig. 4.

	HSS	CIR	CME
P_{dyn} [nPa]	2.72	6.27	11.29
$\lvert B\rvert$ at end of run [nT]	< 1	103	211
σ_B [nT]	19.8	37.1	53.2
Pc4+Pc5 band power [nT^2]	4.0	7.3	141
Maximum dB/dt [nT s^{-1}]	1.88	2.21	1.97
Time of maximum dB/dt [min]	0.6	0.6	0.8

Inner boundary and start-up. The obstacle is a region in which density and pressure are reset at every step, and its thermal pressure (about 17 nPa) exceeds the solar-wind dynamic pressure of all three runs. The continuously re-imposed core and the impulsive start of each run may both affect the solution near the planet. The spike of dB/dt in the first minute, the reversals of B_z and the oscillations of the CIR run should therefore be treated as properties of the model, not as features of the observed magnetospheric response.

Field strength at the station. The field at the station at $t = 0$ is 5–10 nT, whereas the terrestrial dipole field on the dipole axis at 4 R_{E} is roughly 970 nT (Kivelson & Russell, 1995). The model dipole, of strength $B_{\mathrm{d}} = 8$ code units (369 nT on the equator at 1 R_{E}), is thus much weaker than that of the Earth, and its moment is directed along $+x_2$, opposite to the terrestrial dipole. The values in nT and nT s^{-1} are therefore best regarded as relative measures that rank the three regimes, and the station should not be assumed to sample the inner magnetosphere.

Steady, uniform driving and short duration. Each event is reduced to three constants. Real HSS, CIR and CME intervals have shocks, sheaths and rotations of the IMF that last hours to days, whereas each run covers 47 min, and the CME run is still evolving when it ends. The runs therefore represent the onset of driving at a given strength and not the storm.

Drivers and proxies. The upstream values are representative choices, not averages over a defined window of the OMNI record. The index comparison depends on an assumed duration of driving, extrapolates one formulation beyond its range of calibration for the extreme event, and saturates in Kp for that event.

Spectra. The band power is that of a non-stationary transient, as noted above.

These limitations do not affect the main outcome of this work: the pipeline runs from the upstream

doi: https://doi.org/10.52526/25792776-26.73.2-394

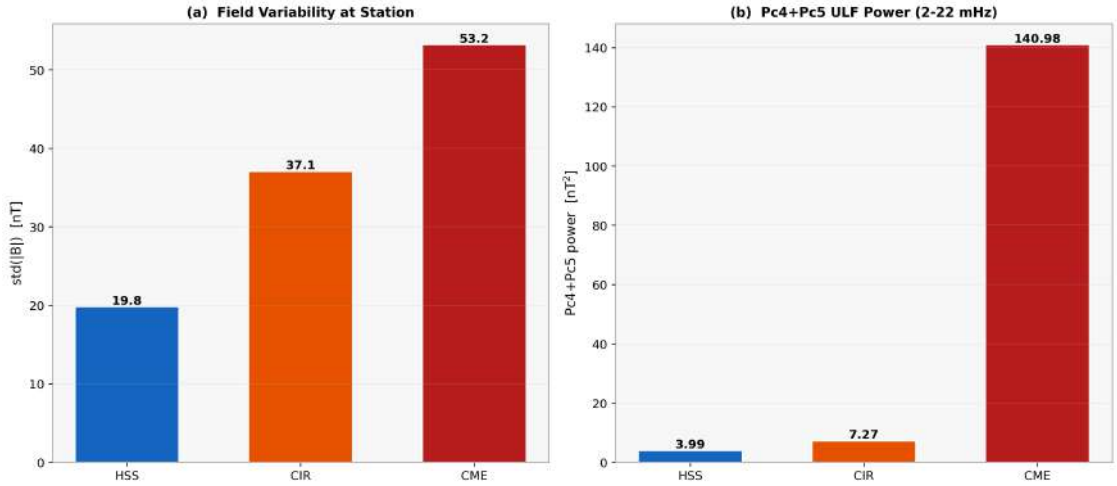

Figure 6. Integrated metrics for the three regimes. (a) Standard deviation of $|B|$ at the station, Eq. (4). (b) Pc4+Pc5 band power, Eq. (5) integrated over 2–22 mHz.

parameters to a set of numerical metrics, each step is specified, and the integrated metrics order the three regimes as the driving does. The present runs do not provide a quantitative estimate of the field variation at the ground during the historical events.

5.2. Future work

Most of the limitations listed above can only be removed in three dimensions. In future work, three-dimensional PLUTO simulations of the same three events will be carried out, with a dipole of terrestrial strength and orientation and a more realistic inner boundary; PLUTO has already been applied in three dimensions to the terrestrial magnetosphere under extreme solar wind (Varela et al., 2022). These simulations will allow a direct comparison with the two-dimensional results presented here and will improve the accuracy of the exposure metrics.

The metrics defined here can then be used to test the arrhythmia hypothesis with a case-crossover analysis of ICD therapy records, in which the exposure of each patient at the time of an event is compared with the same patient's exposure at control times. Since the existing device-based evidence points to fewer therapies on disturbed days (Ebrille et al., 2015, Stoupel, 2006), such a test must be two-sided: events may cluster around peaks of exposure, be depleted there, or show no relation. For that design the present work provides the candidate metrics (σ_B, band-limited power, dB/dt and the index proxies) and the finding that integrated metrics are more robust than single extreme values. Whether the model-derived metrics add information beyond the observed indices remains to be tested.

6. Conclusions

We have presented two-dimensional MHD simulations of three historical solar-wind regimes, together with a pipeline that converts the solar-wind conditions and the simulated field into candidate exposure metrics for studies of geomagnetic disturbance and health. The main results are as follows.

1) Steady drivers representing an HSS (26 August 1992), a CIR (November 1993) and a CME (8–9 November 1991) are consistent with the observed severity of the events. Dst proxies computed from the inputs give −35 nT against an observed −40 nT for the HSS and −313 nT against −354 nT for the CME, and bracket the observed −50 nT of the CIR for driving durations of 4–12 h. The Kp proxy reproduces the HSS value to within half a Kp unit, lies 0.4–1.4 units above the CIR values and saturates for the CME event.

2) On the snapshot cadence and along the dipole axis, the enhancement of the rate of change of the field next to the inner boundary is confined to distances below about 2 R_E; at the station at 4 R_E it is at least eight times smaller than at the edge of the boundary.

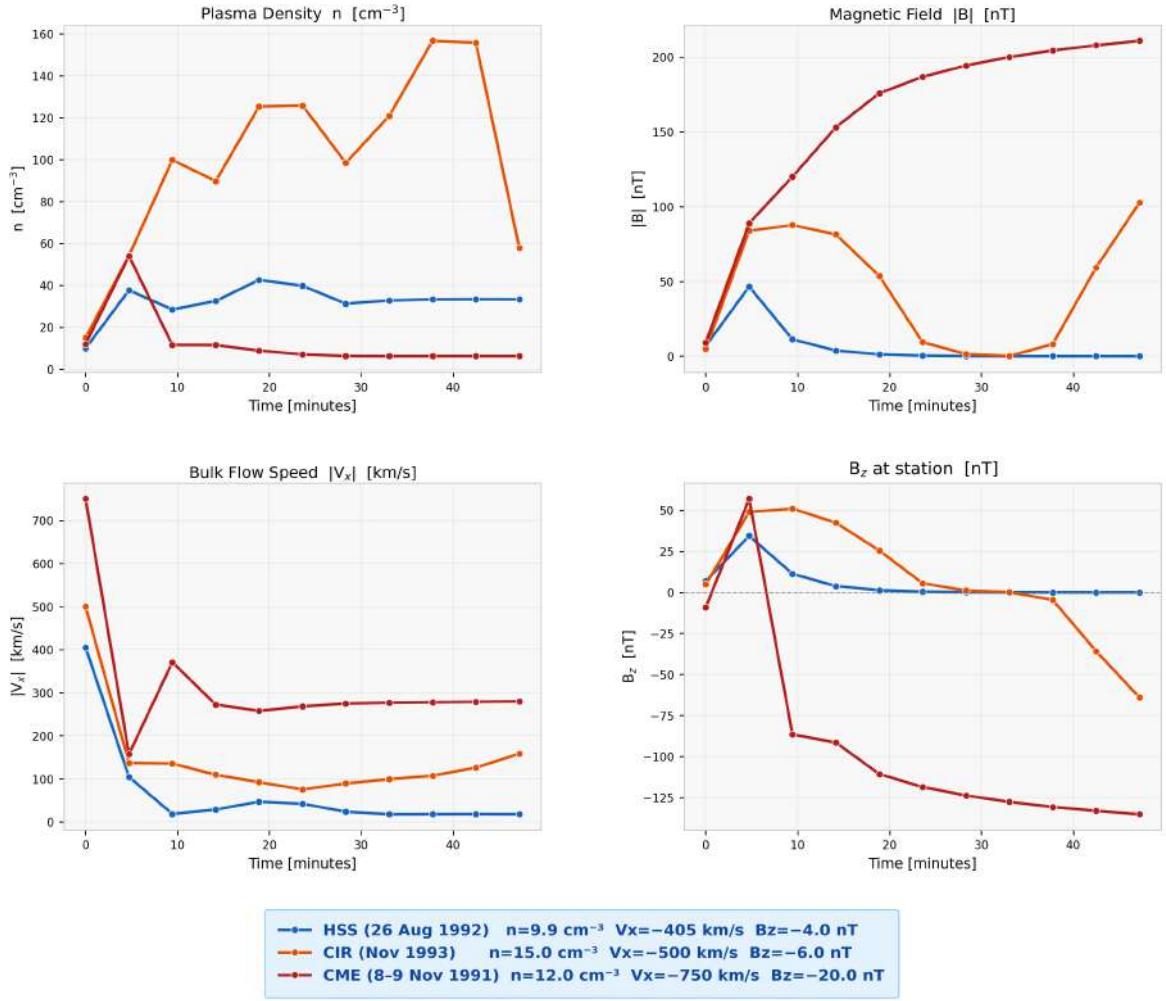

Figure 7. Plasma density n, field magnitude $|B|$, flow speed $|V_x|$ and signed B_z at the diagnostic station from the 11 snapshots of each run (cadence 283 s). The key gives the upstream values of each regime.

3) The integrated metrics order the regimes as the driving does: σ_B = 19.8, 37.1 and 53.2 nT and Pc4+Pc5 band power of 4.0, 7.3 and 141 nT^2 for the HSS, CIR and CME runs.

4) The maximum dB/dt, 1.9–2.2 nT s^{-1} in the first minute of every run, does not follow the driving. We attribute it to the start-up of the simulation and do not regard it as a measure of severity.

5) The model is two-dimensional, uses an idealised inner boundary and steady driving, and covers 47 min. Its metrics rank the regimes but do not reproduce the ground-level field variations of the historical events.

This paper does not test whether geomagnetic disturbances affect cardiac arrhythmia; it provides physically based exposure metrics with which such a test can be carried out.

Author contributions

S. Shamyar conceived the study as part of her doctoral research, defined the exposure metrics and the index-proxy analysis, analysed the station data, related the results to the clinical question and wrote the manuscript. M. Rah designed and performed the PLUTO simulations and mentored the work. A. G. Yeghikyan, as the scientific supervisor of S. Shamyar's doctoral research, defined the research direction of the work, provided scientific guidance and supervision at every stage of the work, and critically reviewed the manuscript.

Acknowledgements

MR and SS thank the staff of the Byurakan Astrophysical Observatory for their hospitality. This paper is based on a talk given at the International Symposium "Our Unstable Universe", dedicated to the 80th anniversary of the Byurakan Astrophysical Observatory (Armenia, 14–18 September 2026). We thank the participants of the 17th International Solar Wind Conference for their comments on the pilot study. We acknowledge the use of the PLUTO code, of the OMNI data of the NASA/GSFC Space Physics Data Facility, of the Dst index of the World Data Center for Geomagnetism, Kyoto, and of the Kp index of GFZ Potsdam.

References

Alabdulgader A., McCraty R., Atkinson M., Dobyns Y., Vainoras A., Ragulskis M., Stolc V., 2018, Scientific Reports, 8, 2663

Borovsky J. E., Denton M. H., 2006, J. Geophys. Res., 111, A07S08

Boteler D. H., Pirjola R. J., Nevanlinna H., 1998, Adv. Space Res., 22, 17

Burton R. K., McPherron R. L., Russell C. T., 1975, J. Geophys. Res., 80, 4204

Ebrille E., et al., 2015, Mayo Clinic Proceedings, 90, 202

Fenrich F. R., Luhmann J. G., 1998, Geophys. Res. Lett., 25, 2999

Franco A. M. S., Rawat R., Bolzan M. J. A., Echer E., 2026, Annales Geophysicae, 44, 881

Gonzalez W. D., Joselyn J. A., Kamide Y., Kroehl H. W., Rostoker G., Tsurutani B. T., Vasyliunas V. M., 1994, J. Geophys. Res., 99, 5771

Harten A., Lax P. D., van Leer B., 1983, SIAM Rev., 25, 35

Jacobs J. A., Kato Y., Matsushita S., Troitskaya V. A., 1964, J. Geophys. Res., 69, 180

Kataoka R., Ngwira C., 2016, Progress in Earth and Planetary Science, 3, 23

Kepko L., Spence H. E., Singer H. J., 2002, Geophys. Res. Lett., 29, 1197

King J. H., Papitashvili N. E., 2005, J. Geophys. Res., 110, A02104

Kivelson M. G., Russell C. T., 1995, Introduction to Space Physics. Cambridge University Press, Cambridge

Knipp D. J., et al., 1998, J. Geophys. Res., 103, 26197

Liu Y. D., Hu H., Zhao X., Chen C., Wang R., 2024, Astrophys. J. Lett., 974, L8

Maclure M., 1991, American Journal of Epidemiology, 133, 144

Mathie R. A., Mann I. R., 2001, J. Geophys. Res., 106, 29783

Matzka J., Stolle C., Yamazaki Y., Bronkalla O., Morschhauser A., 2021, Space Weather, 19, e2020SW002641

McCraty R., Atkinson M., Stolc V., Alabdulgader A. A., Vainoras A., Ragulskis M., 2017, International Journal of Environmental Research and Public Health, 14, 770

Mignone A., Bodo G., Massaglia S., Matsakos T., Tesileanu O., Zanni C., Ferrari A., 2007, Astrophys. J. Suppl. Ser., 170, 228

Mignone A., Zanni C., Tzeferacos P., van Straalen B., Colella P., Bodo G., 2012, Astrophys. J. Suppl. Ser., 198, 7

Newell P. T., Sotirelis T., Liou K., Meng C.-I., Rich F. J., 2007, J. Geophys. Res., 112, A01206

Newell P. T., Sotirelis T., Liou K., Rich F. J., 2008, J. Geophys. Res., 113, A04218

Nose M., Iyemori T., Sugiura M., Kamei T., 2015, Geomagnetic Dst index, World Data Center for Geomagnetism, Kyoto, doi:10.17593/14515-74000

O'Brien T. P., McPherron R. L., 2000, J. Geophys. Res., 105, 7707

Powell K. G., Roe P. L., Linde T. J., Gombosi T. I., De Zeeuw D. L., 1999, J. Comput. Phys., 154, 284

Pulkkinen A., et al., 2013, Space Weather, 11, 369

Pulkkinen A., Bernabeu E., Thomson A., et al. 2017, Space Weather, 15, 828

Rich D. Q., Schwartz J., Mittleman M. A., Link M., Luttmann-Gibson H., Catalano P. J., Speizer F. E., Dockery D. W., 2005, American Journal of Epidemiology, 161, 1123

Saxon L. A., et al., 2010, Circulation, 122, 2359

Shamyar S., Rah M., Yeghikyan A., Khachatryan S., Darbinyan L., 2026, PLUTO MHD pipeline for synthetic mid-latitude ULF signatures and rate of change of magnetic field (dB/dt) GMD, Poster 2-087, 17th International Solar Wind Conference (Solar Wind 17), Bath, UK, 14–19 June 2026

Stoupel E., 2006, Indian Pacing and Electrophysiology Journal, 6, 49

Takahashi K., Ukhorskiy A. Y., 2007, J. Geophys. Res., 112, A11205

Tsurutani B. T., Gonzalez W. D., Gonzalez A. L. C., et al. 2006, J. Geophys. Res., 111, A07S01

Varela J., Brun A. S., Strugarek A., Réville V., Zarka P., Pantellini F., 2022, Astron. Astrophys., 659, A10

Viljanen A., Nevanlinna H., Pajunpää K., Pulkkinen A., 2001, Annales Geophysicae, 19, 1107

Welch P. D., 1967, IEEE Transactions on Audio and Electroacoustics, 15, 70

Zilli Vieira C. L., Alvares D., Blomberg A., Schwartz J., Coull B., Huang S., Koutrakis P., 2019, Environmental Health, 18, 83